Glutamate induces *de novo* growth of functional spines in developing cortex

Hyung-Bae Kwon & Bernardo L. Sabatini

Mature cortical pyramidal neurons receive excitatory inputs onto small protrusions emanating from their dendrites called spines. Spines undergo activity-dependent remodelling, stabilization and pruning during development, and similar structural changes can be triggered by learning and changes in sensory experiences[1–4]. However, the biochemical triggers and mechanisms of *de novo* spine formation in the developing brain and the functional significance of new spines to neuronal connectivity are largely unknown. Here we develop an approach to induce and monitor *de novo* spine formation in real time using combined two-photon laser-scanning microscopy and two-photon laser uncaging of glutamate. Our data demonstrate that, in mouse cortical layer 2/3 pyramidal neurons, glutamate is sufficient to trigger *de novo* spine growth from the dendrite shaft in a location-specific manner. We find that glutamate-induced spinogenesis requires opening of NMDARs (*N*-methyl-D-aspartate-type glutamate receptors) and activation of protein kinase A (PKA) but is independent of calcium–calmodulin-dependent kinase II (CaMKII) and tyrosine kinase receptor B (TrkB) receptors. Furthermore, newly formed spines express glutamate receptors and are rapidly functional such that they transduce presynaptic activity into postsynaptic signals. Together, our data demonstrate that early neural connectivity is shaped by activity in a spatially precise manner and that nascent dendrite spines are rapidly functionally incorporated into cortical circuits.
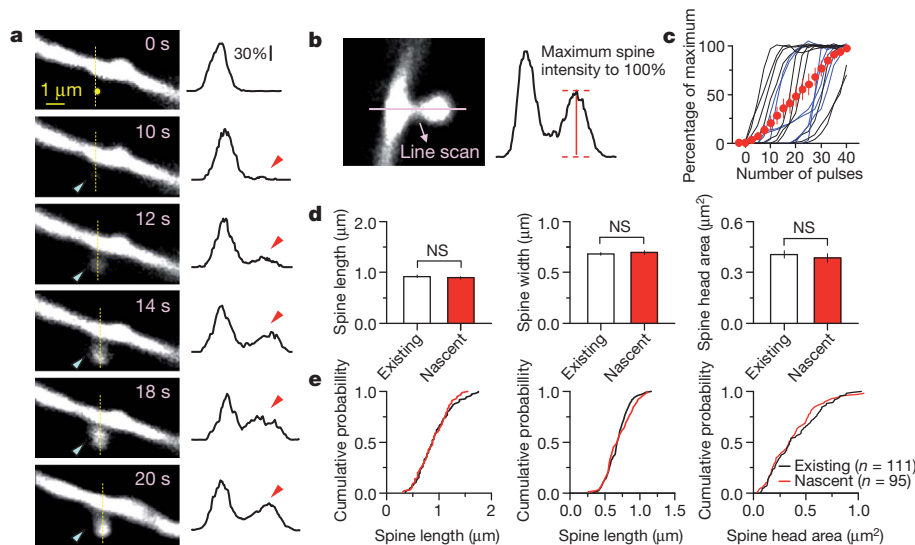
During postnatal development, the formation and elimination of glutamatergic synapses are thought to be reflected in the growth and retraction of dendritic spines. In cortical pyramidal neurons, waves of new spine growth (spinogenesis) and synapse formation (synaptogenesis) occur at specific developmental stages, followed by pruning as the brain matures[5]. Many signals have been proposed to trigger and regulate *de novo* spine growth in a developing circuit including neurotrophins, neurotransmitters and cell-adhesion molecules[6–9]. To uncover the triggers for and mechanisms of spinogenesis, we imaged dendrites of enhanced green fluorescent protein (EGFP)-expressing cortical layer 2/3 pyramidal neurons while releasing glutamate at a specific dendritic location by two-photon laser-induced photolysis of (4-methoxy-7-nitroindolinyl)-glutamate (MNI-glutamate) (Fig. 1). Analysis was performed in acute cortical brain slices from young mice (postnatal day (P) 8–12), a period in which spinogenesis occurs *in vivo*[10].

Stimulation near the edge of a dendrite with 40 0.5-ms laser pulses at 0.5 Hz in a Mg^{2+}-free extracellular solution induced growth of a new spine in approximately 14% of cases (Fig. 1a–d and Supplementary Fig. 1), showing the possibility of *de novo* spinogenesis induced by glutamate exposure[11]. Increasing stimulation frequency and laser pulse duration while maintaining the total number of stimuli at 40 increased the rate of spinogenesis such that, at 5 Hz with 4 ms duration, a maximal success rate of approximately 50% was achieved (Fig. 1c). Nascent spines arose from the dendrite where glutamate was released with high specificity (Fig. 1b) such that more than 70% of them grew within 1 µm of the uncaging spot (Fig. 1e) and 94% of them grew on the side of the dendrite exposed to glutamate.

In 128 of 132 examples of glutamate-induced spinogenesis, the spine was seen to emerge without a filopodial stage (see Supplementary Fig. 2a for an exception). Instead, spine growth occurred incrementally but explosively such that the spine head volume increased from 10 to 90% of maximum within 11.8 ± 1.5 pulses of glutamate (5.9 ± 0.8 s at 2 Hz stimulation) (Fig. 2a–c and Supplementary Fig. 3). The final sizes and lengths of the newborn spines were heterogeneous but not different from those of pre-existing neighbouring spines (Fig. 2d, e). The lifetime of newly formed spines was variable such that approximately 20% lasted less than 2 min but those that lasted 5 min were stable and remained for at least 30 min (Supplementary Fig. 4). Thus, these newly formed spines either did not require continued exposure to glutamate for maintenance or they received glutamate from an alternative source such as an axonal bouton.
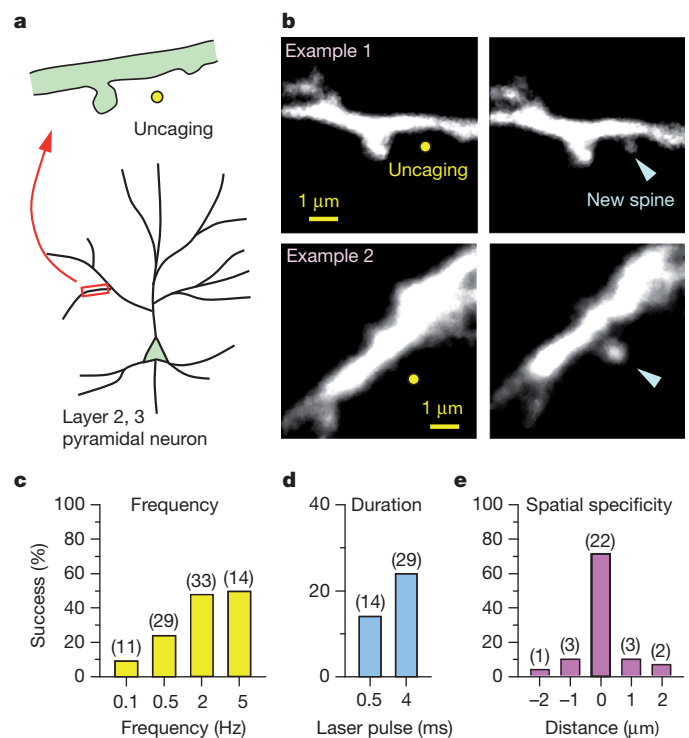
Figure 1 | *De novo* spine generation is induced by glutamate uncaging. **a**, Dendrites of EGFP-expressing neurons in acute slices from P8–12 mice were visualized with two-photon laser scanning microscopy, and glutamate was released by photolysis of caged glutamate near a low-spine density section of dendrite. **b**, Examples of *de novo* spine formation induced by photolytic release of glutamate (40 pulses of MNI-glutamate uncaging at 2 Hz in Mg^{2+}-free artificial cerebrospinal fluid). Yellow circles, the uncaging spots; arrowheads, new spines. **c–e**, Most new spines grew near the uncaging spot and the success percentage depended on the frequency (**c**, laser pulse duration = 4 ms) and duration (**d**, stimulation frequency = 0.5 Hz) of glutamate uncaging. Experiment numbers for each bar are indicated in parentheses.

Howard Hughes Medical Institute, Department of Neurobiology, Harvard Medical School, Boston, Massachusetts 02115, USA.

Figure 2 | New spines grow rapidly and acquire morphology similar to pre-existing spines. a, Left, time-lapse images of spine formation during glutamate uncaging (40 pulses, 2 Hz) showing the uncaging spot (yellow circle) and nascent spine (blue arrowhead). Right, fluorescence intensity profiles along the yellow line reveal that the spine head fluorescence increases gradually but rapidly (red arrowhead). **b**, Illustration of the measurement of spine head fluorescence during spinogenesis as a percentage of the maximum fluorescence intensity reached. **c**, Time course of individual (black, 2 Hz; blue, 0.5 Hz) and average (red) fluorescence intensity increases during spinogenesis ($n = 17$). Error bars, s.e.m. **d**, Average of apparent spine length, width and head area from nascent ($n = 95$) and neighbouring existing ($n = 111$) spines (existing and nascent: length: 0.92 ± 0.03 μm, 0.89 ± 0.03 μm, $P > 0.1$; width: 0.68 ± 0.02 μm, 0.70 ± 0.02 μm, $P > 0.1$; head area: 0.41 ± 0.02 μm^2, 0.38 ± 0.03 μm^2, $P > 0.1$). **e**, Cumulative distributions demonstrating that the morphologies of pre-existing and nascent spines are not different.

Glutamate-induced spinogenesis was restricted within postnatal developmental such that its efficiency diminished by P14–15 and it failed to occur by P19–20 (Supplementary Fig. 5). This was not due to decreased glutamate receptor activation in older animals because the uncaging-evoked excitatory postsynaptic current (uEPSC) was larger at P19–20 than at P10–12 (Supplementary Fig. 6).

Previous ultrastructural studies have revealed a high frequency of dendrite shaft synapses in hippocampus in early postnatal life that decreases as spinogenesis occurs[12], leading to a model of synaptic development in which synapses are initially formed directly onto the dendritic shaft and a spine subsequently grows from this point with the synapse attached. On the other hand, rapid movement of a physically connected spine head and axonal bouton together through a complex neuropile is difficult to reconcile with the high density of crossing axons and dendrites[13]. Our data demonstrate that glutamate uncaging-induced spinogenesis occurs with high spatial specificity and probability on the side of the dendrite exposed to glutamate. These findings place a lower limit of approximately 1 μm^{-1} for the density of dendritic shaft synapses required to support this model of spinogenesis. To estimate the number of dendritic shaft synapses, Ca^{2+} imaging was performed in conditions in which most synapses formed onto a stretch of dendrite were activated (approximately 90%, Supplementary Fig. 7). Under these conditions, we observed hotspots of Ca^{2+} influx in spineless stretches of dendrite at a density of 0.05 μm^{-1}. This corresponds to a density of dendritic shaft synapses containing NMDARs that is approximately 20-fold less than necessary to explain the specificity and efficiency of glutamate-induced spinogenesis (see Supplementary Fig. 7 for further discussion).

The high success rate of spinogenesis induced by glutamate uncaging allows identification of the signalling pathways that couple activity to spine growth (Fig. 3). Previous analyses of spine generation induced by electrical stimulation indicate a requirement for NMDARs in this process[14,15], and at this age NMDARs are found throughout the dendrite (Supplementary Fig. 8). Preventing NMDAR activation with the antagonist 3-(2-carboxypiperazin-4-yl)propyl-1-phosphonic acid (CPP) nearly abolished spinogenesis whereas it was unaffected by inhibiting α-amino-3-hydroxy-5-methyl-4-isoxazole propionic acid (AMPA)/ kainate glutamate receptors with 2,3-dihydroxy-6-nitro-7-sulfamoyl-benzo[f]quinoxaline-2,3-dione (NBQX) (Fig. 3a). The voltage-gated sodium channel antagonist tetrodotoxin also did not affect spinogenesis, discarding the possibility that postsynaptic action potentials are necessary. Addition of extracellular Mg^{2+} significantly decreased the success rate, suggesting that the degree of current flux through NMDARs plays a crucial role in triggering spine formation. Blocking either mGluR1 or mGluR5 using 7-hydroxyiminocyclopropan[b] chromen-1a-carboxylic acid ethyl ester (CPCCOEt) or 2-methyl-6-(phenylethynyl)-pyridine (MPEP) or with the less selective group I mGluR antagonist 1-aminoindan-1,5-dicarboxylic acid (AIDA) demonstrated that neither was strictly necessary for spinogenesis. Lastly, depleting Ca^{2+} stores with cyclopiazonic acid or thapsigargin significantly inhibited spine formation. Thus our data indicate that NMDARs, with additional contributions from intracellular stores provide, the coupling between glutamate and activation of intracellular pathways responsible for spinogenesis.

We further considered intracellular signalling pathways that might be activated in a spatially delimited fashion by glutamate and could provide the spatial information necessary for local spine growth. Previous studies of long-term potentiation and associated spine enlargement in older animals demonstrated a need for activation of CaMKII or signalling by neurotrophin receptor tyrosine kinases such as the BDNF receptor TrkB[16–19]. However, we found that activity-dependent spinogenesis is unaffected by the kinase inhibitors KN-62, KN-93 and K252a, indicating independence from CaMKII and TrkB signalling (Fig. 3a).

The cyclic AMP (cAMP)-activated kinase PKA is required for long-term potentiation induction in younger neurons[20], and gradients in its concentration can be maintained over micrometre-length scales[21]. Raising cAMP concentration by applying the adenylate cyclase activator forskolin was not sufficient to generate spines on its own ($n = 3$, data not shown), but glutamate uncaging in its presence increased the spinogenesis success rate to approximately 80% (Fig. 3a). In the presence of forskolin, multiple spines often grow with each induction attempt (Fig. 3b, c), including at sites more distant from the uncaging location (Fig. 3d). In addition, the PKA inhibitor H-89 prevented new
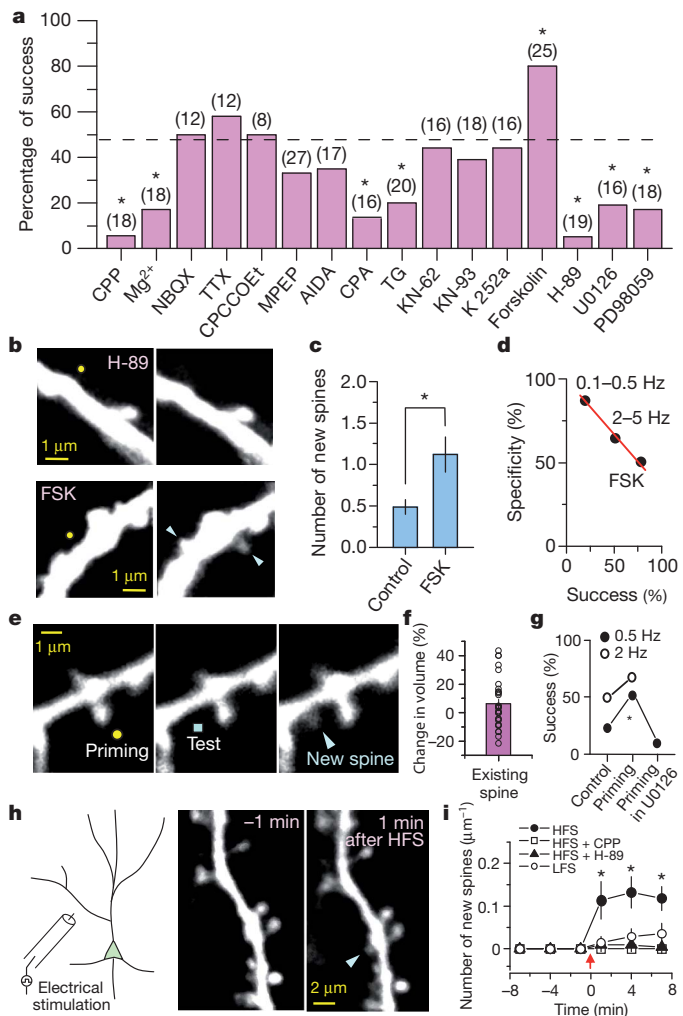
Figure 3 | Molecular mechanisms of glutamate-induced spine formation.
a, Spine formation using the 40 pulses at 2 Hz protocol was tested in the
presence of pharmacological agents. The dotted line indicates the success
percentage in control conditions with which statistical comparison was made.
The number of induction attempts for each condition is given in parentheses,
and the numbers of successes and total trials are summarized in Supplementary
Table 2. TG, thapsigargin; CPA, cyclopiazonic acid. **b**, Examples of blockade of
spine generation and of exuberant spine growth. Images taken before (left) and
after (right) glutamate uncaging in the presence of either H-89 or forskolin
(FSK). Arrowheads, nascent spines. **c**, Summary of the average number of new
spines with each induction attempt (control: 0.48 ± 0.09, $n = 33$; FSK:
1.12 ± 0.21, $n = 25$, $P < 0.005$). **d**, Inverse relation between the location
specificity and success rate. Data from three groups (0.1–0.5 Hz, 2–5 Hz and
FSK at 2 Hz) are plotted. Specificity was measured as the percentage of cases in
which the spine arose within 1 μm of the uncaging spot. **e**, Representative
images of priming experiments in which 40 pulses of 2 Hz glutamate uncaging
were delivered to a pre-existing spine (yellow circle) followed by an additional
40 pulses (0.5 Hz or 2 Hz) delivered to the nearby dendrite (blue square).
Releasing glutamate did not cause enlargement of the pre-existing spine head
(left), but did trigger new spine growth from the dendrite (middle, right).
f, Changes in the fluorescence of pre-existing spine heads exposed to the
priming stimulus (individual spines: circles; bar graph: average $\pm$ s.e.m.)
($n = 31$). **g**, Percentage of successful spine generation at the indicated test
frequencies with and without priming. U0126 prevented spinogenesis
facilitated by the priming protocol. **h**, The experiment (left) and images of a
dendrite 1 min before (middle) and after (right) HFS (2×100 pulses at
100 Hz). **i**, Average numbers of new spines generated by HFS per micrometre of
dendrite in control conditions (at 7 min: 0.12 ± 0.03, $n = 11$, $P < 0.005$), in the
presence of CPP (0, $n = 8$, $P > 0.5$), or H-89 (0.004 ± 0.001, $n = 12$; $P > 0.5$).
The same number of pulses at a lower frequency (LFS, 10 Hz) generated fewer
new spines (0.035 ± 0.024, $n = 7$, $P > 0.1$). Error bars, s.e.m.

spine growth (Fig. 3a), indicating that PKA activity is necessary but not
sufficient for spinogenesis.

The small guanosine triphosphatase Ras is activated by Ca^{2+} influx
through NMDARs and signals through mitogen-activated protein kinase
(MAPK) to promote long-term potentiation[17,22]. We found that the
MAPK pathway was necessary for spinogenesis because the success rate
was significantly reduced by blocking the upstream activator MAPK
kinase 1/2 (MEK1/2) with U0126 or MEK1 with PD98059 (Fig. 3a).
In pyramidal neurons, activated Ras diffuses from active spines to
neighbouring spines and heterosynaptically facilitates plasticity[17].
To examine if a similar phenomenon potentiates spinogenesis, we
delivered a 'priming' stimulus to a pre-existing spine (40 pulses at
2 Hz, Fig. 3e) and then a 'test' stimulus to the dendritic shaft within
1–2 min. In contrast to previous studies of older neurons in hip-
pocampus[16–18], we found no consistent increase in volume of the exist-
ing spine in response to this priming stimulus (Fig. 3f), supporting the
idea that spinogenesis is not simply due to the growth of an undetect-
able pre-existing spine. Nevertheless, the success rate of spine genera-
tion was enhanced by the priming stimulus in a MEK1/2-dependent
manner such that the low level of spinogenesis evoked by a 0.5 Hz test
stimulus was increased. In contrast, the priming stimulus did not
increase the success rate when the test stimulus was delivered at
2 Hz (Fig. 3g), indicating that the priming protocol shifted the induc-
tion threshold for spinogenesis.

With the exception of the NMDAR and PKA antagonists, none of the
pharmacological manipulations that altered spinogenesis rates affected
dendritic currents or Ca^{2+} transients (Supplementary Fig. 8). As
expected, CPP largely abolished the Ca^{2+} transient and the prolonged
phase of the currents. Consistent with a facilitation of Ca^{2+} influx
through NMDARs by PKA[23,24], H-89 lowered dendritic Ca^{2+} transients
by approximately 20% (Supplementary Table 1). However, this effect is
insufficient to explain the near abolition of spinogenesis because the
rate of spinogenesis evoked by 0.5 ms uncaging pulses in control con-
ditions was higher than that evoked by 4 ms pulses in H-89, despite
eliciting smaller dendritic Ca^{2+} transients (Supplementary Fig. 8 and
Supplementary Table 1).

We examined whether endogenous synaptic activity generates new
spines in cortical tissue from young mice through similar pathways. In
normal extracellular Mg^{2+}, high-frequency (100 pulses at 100 Hz,
delivered twice, separated by 10 s) but not low-frequency (10 Hz) elec-
trical tetani rapidly triggered new spine growth (Fig. 3h, i). Blockade of
NMDARs or PKA prevented this synaptically evoked spine growth
(Fig. 3i) as well as spontaneous new spine growth that occurred when
NMDAR activation was increased by removing extracellular Mg^{2+}
and blocking inhibitory $GABA_A$ receptors (Supplementary Fig. 9).
Hence, multiple experimental models demonstrate that activity-
dependent spinogenesis in developing cortex requires NMDAR- and
PKA-dependent signalling.

To determine if nascent spines detect synaptically released glutam-
ate and are functionally incorporated into the circuit, we generated
new spines by high-frequency stimulation (HFS) and examined their
synaptic responses using optical quantal analysis of synaptic properties.
A whole-cell recording was obtained and the probability and amplitude
of synaptically evoked NMDAR-mediated Ca^{2+} transients in the spine
head were monitored (Fig. 4a). Using the Ca^{2+}-sensitive green fluor-
ophore Fluo-5F, we detected stimulus-evoked Ca^{2+} transients in the
heads of newly grown spines (Fig. 4b, c), demonstrating that they sense
synaptic activity within a neural circuit within 30 min after growth.
Similar results were obtained in five of seven new spines and in 11 of
16 pre-existing spines. Analysis of the spines in which an evoked Ca^{2+}
transient could be detected indicated that nascent spines displayed
smaller and less frequent synaptically evoked Ca^{2+} transients than
pre-existing spines (Fig. 4d, e). Similar results were obtained for new
spines that grew in response to glutamate uncaging and were probed
using a glass-stimulating electrode placed near the spine (Supplemen-
tary Fig. 10).
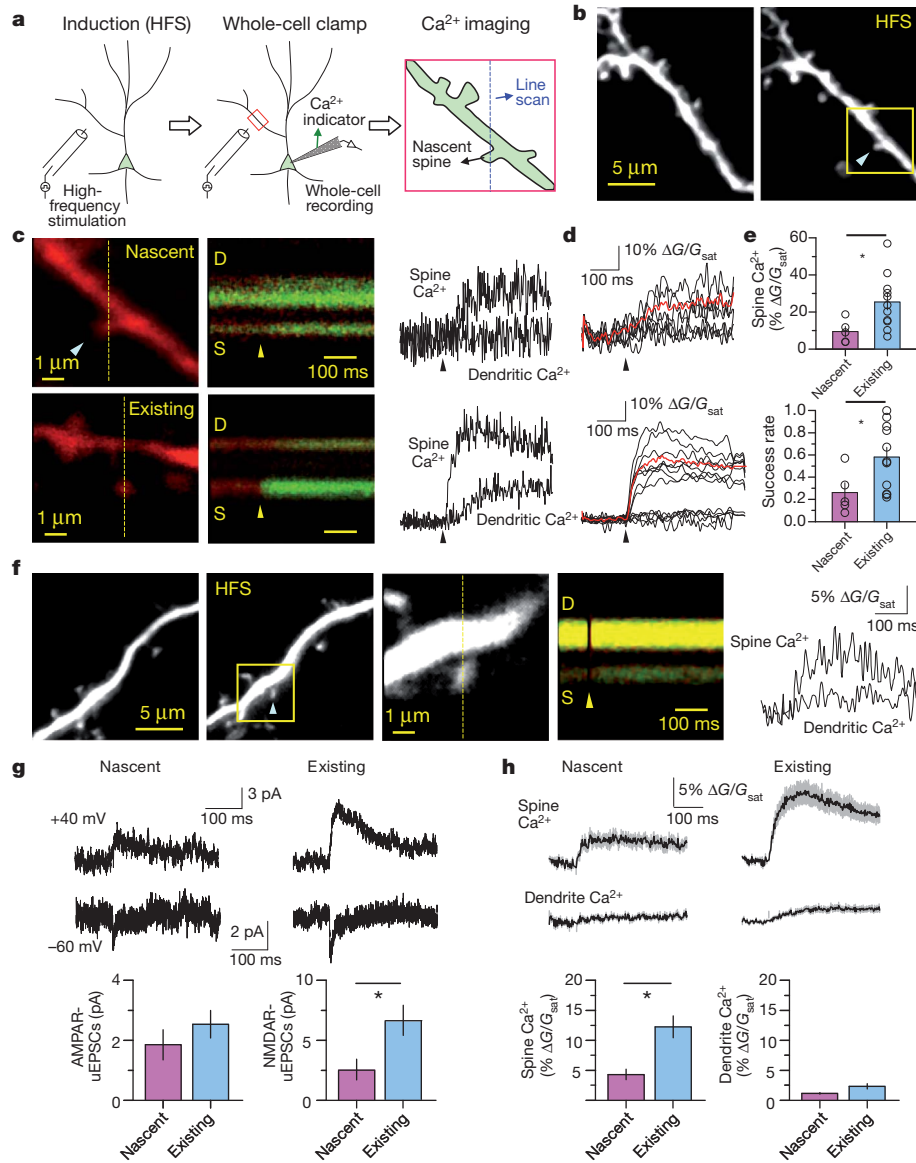
Figure 4 | Functional characterization of new spines. a, Schematic of the experimental procedure. HFS was delivered approximately 30 μm from the target dendritic region (red box). After nascent spines were identified, Ca^{2+} indicator was loaded into the cell through a whole-cell recording pipette. The newly generated spine was examined at higher temporal and spatial resolution to measure synaptically evoked Ca^{2+} transients in the spine head and perform optical quantal analysis. **b**, Images before and after HFS showing the new spine (arrowhead) and the area subsequently analysed at higher resolution (yellow box). **c**, Images (left) of newly generated spines (top) and pre-existing (bottom) spines filled with the fluorophore Alexa 594 (red, 20 μM) and Fluo-5F (green, 300 μM). Fluorescence was collected (middle) and quantified (right) from a line-scan intersecting the spine (S) and dendrite (D) after electrical stimulation (arrowhead). The increases in green fluorescence indicate Ca^{2+} entry. **d**, Green fluorescence transients collected in consecutive trials (black) showing successes and failures. The average 'success' fluorescence transient is also shown (red).

e, Average amplitude (top, $\Delta G/G_{sat}$) and rate (bottom) of success trials in nascent and neighbouring existing spines for neurons held at -60 mV (nascent and existing: spine Ca^{2+} $\Delta G/G_{sat}$: 9.45 ± 2.8%, $n = 5$, 25.5 ± 4.4%, $n = 11$, $P < 0.05$; success rate: 0.26 ± 0.09, $n = 5$, 0.58 ± 0.09%, $n = 11$, $P < 0.05$). **f**, Similar experiments as those in **a–c** using glutamate uncaging to characterize the glutamate receptors on the nascent spine. **g**, Examples (top) and average amplitudes (bottom) of AMPAR- and NMDAR-mediated uEPSCs at holding potentials of -60 and $+40$ mV, respectively, using 1 ms uncaging pulses (nascent and existing: AMPAR-uEPSC: $-1.9 ± 1.4$ pA, $n = 8$, $-2.5 ± 0.5$ pA, $n = 18$, $P > 0.05$; NMDAR-uEPSC: 2.5 ± 1.4 pA, $n = 8$, 6.3 ± 1.3 pA, $n = 18$, $P < 0.05$). **h**, Average Ca^{2+} transients measured in spine heads and dendrites for neurons held at -60 mV (nascent and existing: spine Ca^{2+} $\Delta G/G_{sat}$: 4.3 ± 0.9%, $n = 8$, 12.3 ± 1.8%, $n = 18$, $P < 0.05$; dendrite Ca^{2+} $\Delta G/G_{sat}$: 1.1 ± 0.1%, $n = 8$, 2.3 ± 0.4%, $n = 18$, $P > 0.05$). Error bars, s.e.m.

The AMPA receptor (AMPAR) and NMDAR content of new spines was characterized using glutamate uncaging after HFS-induced spinogenesis. In all cases, we detected fast uEPSCs at a holding potential of -60 mV and large prolonged uEPSCs at $+40$ mV (Fig. 4g), consistent with AMPAR- and NMDAR-mediated currents previously characterized in these cells[25]. Similarly, uncaging-evoked Ca^{2+} transients were clearly visible at -60 mV (Fig. 4h) but were larger at $+40$ mV (data not shown), consistent with the known properties of NMDAR-mediated Ca^{2+} influx. Despite similar-sized AMPAR-uEPSCs in new and pre-existing spines, NMDAR-uEPSCs and Ca^{2+} influx were significantly lower in nascent

than pre-existing spines (Fig. 4g, h), similar to previous descriptions of spontaneously appearing new spines in hippocampal organotypic slices[26]. Therefore the smaller Ca^{2+} transients measured in nascent spines by synaptic activation probably reflect a smaller number of postsynaptic NMDARs.

In this study, we established a protocol for the reliable and spatiotemporally precise induction of spinogenesis. These experiments demonstrate that glutamate is sufficient to trigger rapid spine formation and suggest that neurons use glutamate release to establish circuit wiring. Thus these data support the hypothesis that axonal growth and

glutamate release may be the triggering event in synapse formation such that axonal bouton localization is an important early step for precise neuronal circuit formation[10,27]. Given the involvement of NMDARs, Ca^{2+} stores, cAMP, PKA and MAPK in activity-dependent spinogenesis, it is likely that many neuromodulators that regulate these molecules may influence the capacity or threshold for new spine formation. For instance, activation of dopaminergic, serotonergic or adrenergic receptors that signal by $G\alpha_s$ may facilitate spinogenesis, whereas receptors that activate $G\alpha_i$-coupled signalling may function as inhibitory signals.

Lastly, we provide experimental evidence that spines that grow *de novo* in developing cortical tissue become rapidly functionally integrated into the circuit such that they sense synaptically released glutamate through AMPARs and NMDARs. Whether these nascent spines are rapidly physically associated with a presynaptic bouton and display the ultrastructural correlates of a synapse is unknown[26,28–30]. Our results indicate that spines can grow *de novo* without the need for a filopodial intermediate and probably without a dendritic-shaft synapse stage. In total, this study demonstrates that synaptic activity can rapidly modify neuronal connectivity with high accuracy by generating new circuit elements.

METHODS SUMMARY

All procedures on animals followed protocols approved by the Harvard Standing Committee on Animal Care and National Institutes of Health guidelines. *In utero* electroporation of EGFP was performed at embryonic day 15.5 in C57BL/6 mice. All studies were performed on layer 2/3 pyramidal neurons in acute coronal slices identified by their characteristic morphology, position in the slice and expression of GFP. Two-photon glutamate uncaging and imaging was performed using custom microscopes. To induce spine growth, 40 uncaging pulses were delivered at varying frequencies to a spot approximately 0.5 μm from the edge of the dendrite. Synaptically induced spine growth was triggered with two high-frequency stimuli (100 pulses at 100 Hz) separated by 10 s delivered by a bipolar electrode positioned approximately 30 μm from the target dendrite. For Ca^{2+} imaging, neurons were loaded through the whole-cell recording electrode with Alexa Fluor-594 (20 μM) and Fluo-5F (300 μM) and the amplitudes of fluorescence transients were quantified as a fraction of the maximal green fluorescence achieved in saturating (sat) Ca^{2+} concentrations (G_{sat}). For optical quantal analysis, the synapse associated with a visualized spine was stimulated using a closely positioned glass electrode. The position of the electrode and stimulus intensity were adjusted until (1) Ca^{2+} transients were evoked in the spine head that demonstrated stochastic failures and successes, and (2) Ca^{2+} transients in other spines and the dendritic shaft in the field of view were not evoked. Fisher's exact test was used to compare the efficacy of spinogenesis across conditions. For each spinogenesis trial, an observer blind to the experimental condition was asked to identify if (1) a new spine had grown and (2), if so, how many spines had grown.

1. Grutzendler, J., Kasthuri, N. & Gan, W. B. Long-term dendritic spine stability in the adult cortex. *Nature* **420**, 812–816 (2002).
2. Hofer, S. B., Mrsic-Flogel, T. D., Bonhoeffer, T. & Hubener, M. Experience leaves a lasting structural trace in cortical circuits. *Nature* **457**, 313–317 (2009).
3. Trachtenberg, J. T. *et al.* Long-term *in vivo* imaging of experience-dependent synaptic plasticity in adult cortex. *Nature* **420**, 788–794 (2002).
4. Zuo, Y., Yang, G., Kwon, E. & Gan, W. B. Long-term sensory deprivation prevents dendritic spine loss in primary somatosensory cortex. *Nature* **436**, 261–265 (2005).
5. Rakic, P., Bourgeois, J. P., Eckenhoff, M. F., Zecevic, N. & Goldman-Rakic, P. S. Concurrent overproduction of synapses in diverse regions of the primate cerebral cortex. *Science* **232**, 232–235 (1986).
6. Dalva, M. B., McClelland, A. C. & Kayser, M. S. Cell adhesion molecules: signalling functions at the synapse. *Nature Rev. Neurosci.* **8**, 206–220 (2007).
7. Scheiffele, P. Cell-cell signaling during synapse formation in the CNS. *Annu. Rev. Neurosci.* **26**, 485–508 (2003).
8. Sudhof, T. C. Neuroligins and neurexins link synaptic function to cognitive disease. *Nature* **455**, 903–911 (2008).
9. Yuste, R. & Bonhoeffer, T. Genesis of dendritic spines: insights from ultrastructural and imaging studies. *Nature Rev. Neurosci.* **5**, 24–34 (2004).
10. Miller, M. & Peters, A. Maturation of rat visual cortex. II. A combined Golgi-electron microscope study of pyramidal neurons. *J. Comp. Neurol.* **203**, 555–573 (1981).
11. Richards, D. A. *et al.* Glutamate induces the rapid formation of spine head protrusions in hippocampal slice cultures. *Proc. Natl Acad. Sci. USA* **102**, 6166–6171 (2005).
12. Fiala, J. C., Feinberg, M., Popov, V. & Harris, K. M. Synaptogenesis via dendritic filopodia in developing hippocampal area CA1. *J. Neurosci.* **18**, 8900–8911 (1998).
13. Sorra, K. E., Fiala, J. C. & Harris, K. M. Critical assessment of the involvement of perforations, spinules, and spine branching in hippocampal synapse formation. *J. Comp. Neurol.* **398**, 225–240 (1998).
14. Engert, F. & Bonhoeffer, T. Dendritic spine changes associated with hippocampal long-term synaptic plasticity. *Nature* **399**, 66–70 (1999).
15. Maletic-Savatic, M., Malinow, R. & Svoboda, K. Rapid dendritic morphogenesis in CA1 hippocampal dendrites induced by synaptic activity. *Science* **283**, 1923–1927 (1999).
16. Harvey, C. D. & Svoboda, K. Locally dynamic synaptic learning rules in pyramidal neuron dendrites. *Nature* **450**, 1195–1200 (2007).
17. Harvey, C. D., Yasuda, R., Zhong, H. & Svoboda, K. The spread of Ras activity triggered by activation of a single dendritic spine. *Science* **321**, 136–140 (2008).
18. Matsuzaki, M., Honkura, N., Ellis-Davies, G. C. & Kasai, H. Structural basis of long-term potentiation in single dendritic spines. *Nature* **429**, 761–766 (2004).
19. Tanaka, J. *et al.* Protein synthesis and neurotrophin-dependent structural plasticity of single dendritic spines. *Science* **319**, 1683–1687 (2008).
20. Yasuda, H., Barth, A. L., Stellwagen, D. & Malenka, R. C. A developmental switch in the signaling cascades for LTP induction. *Nature Neurosci.* **6**, 15–16 (2003).
21. Zaccolo, M. & Pozzan, T. Discrete microdomains with high concentration of cAMP in stimulated rat neonatal cardiac myocytes. *Science* **295**, 1711–1715 (2002).
22. Di Cristo, G. *et al.* Requirement of ERK activation for visual cortical plasticity. *Science* **292**, 2337–2340 (2001).
23. Chalifoux, J. R. & Carter, A. G. GABA_B receptors modulate NMDA receptor calcium signals in dendritic spines. *Neuron* **66**, 101–113 (2010).
24. Skeberdis, V. A. *et al.* Protein kinase A regulates calcium permeability of NMDA receptors. *Nature Neurosci.* **9**, 501–510 (2006).
25. Busetto, G., Higley, M. J. & Sabatini, B. L. Developmental presence and disappearance of postsynaptically silent synapses on dendritic spines of rat layer 2/3 pyramidal neurons. *J. Physiol. (Lond.)* **586**, 1519–1527 (2008).
26. Zito, K., Scheuss, V., Knott, G., Hill, T. & Svoboda, K. Rapid functional maturation of nascent dendritic spines. *Neuron* **61**, 247–258 (2009).
27. Hamori, J. The inductive role of presynaptic axons in the development of postsynaptic spines. *Brain Res.* **62**, 337–344 (1973).
28. De Roo, M., Klauser, P., Mendez, P., Poglia, L. & Muller, D. Activity-dependent PSD formation and stabilization of newly formed spines in hippocampal slice cultures. *Cereb. Cortex* **18**, 151–161 (2008).
29. Nagerl, U. V., Kostinger, G., Anderson, J. C., Martin, K. A. & Bonhoeffer, T. Protracted synaptogenesis after activity-dependent spinogenesis in hippocampal neurons. *J. Neurosci.* **27**, 8149–8156 (2007).
30. Knott, G. W., Holtmaat, A., Wilbrecht, L., Welker, E. & Svoboda, K. Spine growth precedes synapse formation in the adult neocortex *in vivo*. *Nature Neurosci.* **9**, 1117–1124 (2006).

Methods

***In utero* electroporation and DNAs.** All procedures on animals performed in this study followed protocols approved by the Harvard Standing Committee on Animal Care and National Institutes of Health guidelines. Embryonic day (E)15.5~16 timed-pregnant female C57BL/6 mice (Charles River, Massachusetts, United States) were deeply anesthetized with 2% isoflurane. Uterine horns were exposed and periodically rinsed with warm PBS. An EGFP-encoding plasmid (1~1.5 μg/μl) diluted with PBS was injected into the lateral ventricle of one cerebral hemisphere. Five voltage pulses (50 V, 50 ms duration, 1 Hz) were delivered using round plate electrodes (CUY21 electroporator, NEPA GENE, Japan). Injected embryos were placed back into the dam, and allowed to mature to delivery.

Slice preparation. Electroporated mice (postnatal day 8~20) were deeply anesthetized with isoflurane and decapitated. The brain was quickly removed and placed into chilled choline-based cutting solution containing (in mM) 25 $NaHCO_3$, 1.25 NaH_2PO_4, 2.5 KCl, 7 $MgCl_2$, 25 glucose, 1 $CaCl_2$, 110 choline chloride, 11.6 ascorbic acid, and 3.1 pyruvic acid. The brain was cut coronally at 300 µm thickness using a Leica VT1000S vibratome (Leica Instruments, Nussloch, Germany). Slices containing barrel cortex were placed in a glass chamber filled with artificial cerebrospinal fluid (ACSF) containing (in mM) 127 NaCl, 2.5 KCl, 25 $NaHCO_3$, 1.25 NaH_2PO_4, 2 $CaCl_2$, 1 $MgCl_2$ and 25 glucose. Both cutting and ACSF solutions were saturated with 95% O_2 and 5% CO_2. The slices were incubated at room temperature for at least 30 minutes before the experiments and used within 4 hours of cutting. All studies were performed at room temperature.

Two-photon microscope and uncaging. Uncaging of MNI-glutamate and spine/dendrite imaging were achieved by a custom-built microscope combining two-photon laser-scanning microscopy (2PLSM) and two-photon laser photoactivation (2PLP) as previously described[31]. Two Ti:Sapphire lasers

(Chameleon, Coherent, Santa Clara, CA) were used for imaging and uncaging with wavelengths of 840 nm and 720 nm, respectively. The intensity of each laser was independently controlled by Pockels cells (Conoptics, Danbury, CT). For MNI-glutamate uncaging, 5 mM MNI-caged-glutamate was perfused into the slice chamber, and ~50 mW of 720 nm light at the back aperture of the objective (60X 1.10 NA objective, Olympus) was used to release the uncaging group. The laser power measured at the specimen was 10-15 mW. Primary or secondary branches of apical dendrites of layer 2/3 pyramidal neurons were examined and the uncaging position was chosen based on two criteria. First, the outer membrane of the dendrite had to be smooth in the immediate vicinity of the uncaging location. Second, there had to be at least one spine nearby (within 5 μm) in order to ensure that the dendrite was competent for spinogenesis. The uncaging location was approximately 0.5 μm away from the edge of the dendrite. No more than two spinogenesis trials were performed from the same neuron. Spine/dendrite image stacks were taken immediately before and after the induction protocol to minimize the time delay after the induction protocol (less than 1 minute). In order to determine the time course of spine generation, a line crossing the dendrite and the middle of the spine head was drawn and fluorescence intensity along the line was measured using ImageJ (NIH) (see Fig. 2a). Spine head fluorescence was expressed as a percentage of the maximum fluorescence intensity of the spine head reached during the induction protocol.

Electrophysiology and Ca^{2+} imaging. Brain slices were transferred to a recording chamber perfused with Mg^{2+}-free ACSF, except for electrical stimulation experiments (Fig. 3 and 4) in which 1 mM Mg^{2+}-containing ACSF was used. For voltage-clamp recordings, the recording electrode was filled with an internal solution containing (in mM) 120 CsMeSO$_3$, 8 NaCl, 15 CsCl$_2$, 10 TEA·Cl, 10 HEPES, 2 QX-314, 4 MgATP, and 0.3 Na$_2$GTP (pH 7.3). To measure Ca^{2+} from spines and dendrites, Alexa Fluor-594 (20 μM) and Fluo-5F (300 μM) were added to the internal solution. The pipette resistance was 2~4 MΩ and whole-cell recordings were made from cortical layer 2/3 pyramidal neurons. At least 10

minutes were allowed to pass after breaking the cell membrane to allow Ca^{2+} indicator to diffuse into the cell. Electrical tetanic stimuli were given twice at 100 Hz or 10 Hz every 10 seconds using a bipolar stimulation electrode positioned 30~40 μm away from the target dendrite (duration, 0.01 ms; amplitude, 30 V). In control experiments this stimulation produced an EPSC with amplitude 510 ± 62 pA (n=11). To quantify the amplitude of NMDAR-uEPSCs, the current amplitude 50 ms after the uncaging pulse was measured. All recordings were made with a MultiClamp 700A (Axon Instruments Inc., Union City, CA, USA). uEPSC amplitudes were measured from average of 7~15 uncaging pulses delivered to each spine.

In order to determine if a glutamate uncaging induced new spine was associated with a synapse (Supplementary Fig. 10), we performed optical quantal analysis as described previously[23,32-35]. Using this approach, a thin glass electrode is placed near the spine of interest and the position and stimulus intensity of the stimulation is adjusted until a stimulus-evoked Ca^{2+} transient is detected in the spine head. Small stimulation intensities are used (~ 0.3 μA) in order to prevent activation of many axons or direct stimulation of the dendrite. Each spine was stimulated 20~30 times at 0.067 Hz. Lack of direct stimulation is ensured by the presence of stochastic successes and failures of eliciting a Ca^{2+} transient in the head and the lack of a substantial dendritic Ca^{2+} transient. Furthermore, using this assay the Ca^{2+} transient in the spine head is unlikely to result from spill-over and diffusion of glutamate from neighboring synapses because: (1) it demonstrates stochastic failures at a rate higher than that of neighboring synapses, inconsistent with the expected statistics of sampling many synapses; and (2) there is a large gradient in Ca^{2+} between the active spine head and the dendrite which, due to the high number of dendritic NMDARs (Supplementary Fig. 8), indicates a gradient of extracellular glutamate. Furthermore, it is unlikely that the stochastic synaptically-evoked Ca^{2+} transients in nascent spines result from spill-over of glutamate from many neighboring co-active synapses since they would, in such a case, be expected to exhibit lower failure rates than the preexisting spines.

In the cases in which we were unable to evoke any synaptically-evoked Ca^{2+} transients in a spine, it is impossible to conclude if this is because of a lack of an associated presynaptic bouton or because of a failure to position the electrode properly to stimulate the associated axon.

Analysis of spine morphology. Spine head area and length were analyzed using a custom program in MATLAB as described previously[36]. For each spine, one line was drawn along the length of spine (major axis) and a second line (minor axis) was drawn to intersect the first line at the middle of the spine head where the fluorescence intensity was maximal. Spine head area was calculated by counting the number of pixels where fluorescence intensity was above the 30% of the maximal value. Spine length was designated as the 30% drop-off point of the maximum fluorescence along the major axis. Filopodia were defined as a processes >2.5 μm in length lacking a clear spine head.

Images of spines and dendrites were collected at 256 x 256 pixels over a field of view of ~7 microns per side. The images were processed with a 3x3 median filter to reduce shot noise and dark noise counts in the background. Dark noise is estimated at 1 count per ~32 pixels based on a dark count rate of 4000 Hz. The sampling interval oversamples the microscope resolution ~20 fold, thus the 3x3 median filter does not distort the image. The images are displayed using a linear gray-scale look-up table in which black corresponds to the signal measured with the imaging laser shutter closed. This fluorescent-independent signal measured in the dark results from offsets in the photomultiplier tube/trans-impedance amplifier/data acquisition collection system.

Blind evaluation. The success rate of *de novo* spine generation shown in Fig. 1-3 was determined by a neutral observer who was blind to the experimental condition. All images collected before and after the induction protocol were given to the evaluator. The evaluator was asked to examine each section of the image stacks and decide if any new spines had appeared and, if so, how many. If any new spines had appeared, the experiment was labeled as "Success" and all

other cases were labeled as "Failure". The fraction of "Success" cases was calculated for each experimental condition.

Pharmacology and statistics. The concentrations of individual drugs used in Fig. 3a are (in µM): CPP (10), $MgCl_2$ (1000), NBQX (10), TTX (1), CPCCOEt (100), MPEP (4), AIDA (50), Cyclopiazonic acid (30), Thapsigargin (10), KN-62 (10), KN-93 (10), K 252a (0.2), Forskolin (10), H-89 (10), U0126 (10), PD98059 (50). Slices were incubated in each drug for at least 30 min prior to analysis.

The Fisher's exact test was used to determine the significance of differences in success rate across conditions (see Fig. 3). Student's t-test was used for all other comparisons. $p < 0.05$ was considered significant and, in the figures, asterisks denote statistical significance.

Methods references

31   Carter, A. G. & Sabatini, B. L. State-dependent calcium signaling in dendritic spines of striatal medium spiny neurons. *Neuron* **44**, 483-493 (2004).
32   Higley, M. J., Soler-Llavina, G. J. & Sabatini, B. L. Cholinergic modulation of multivesicular release regulates striatal synaptic potency and integration. *Nat Neurosci* **12**, 1121-1128 (2009).
33   Oertner, T. G., Sabatini, B. L., Nimchinsky, E. A. & Svoboda, K. Facilitation at single synapses probed with optical quantal analysis. *Nat Neurosci* **5**, 657-664 (2002).
34   Sabatini, B. L., Oertner, T. G. & Svoboda, K. The life cycle of Ca(2+) ions in dendritic spines. *Neuron* **33**, 439-452 (2002).
35   Soler-Llavina, G. J. & Sabatini, B. L. Synapse-specific plasticity and compartmentalized signaling in cerebellar stellate cells. *Nat Neurosci* **9**, 798-806 (2006).
36   Steiner, P. *et al.* Destabilization of the postsynaptic density by PSD-95 serine 73 phosphorylation inhibits spine growth and synaptic plasticity. *Neuron* **60**, 788-802 (2008).
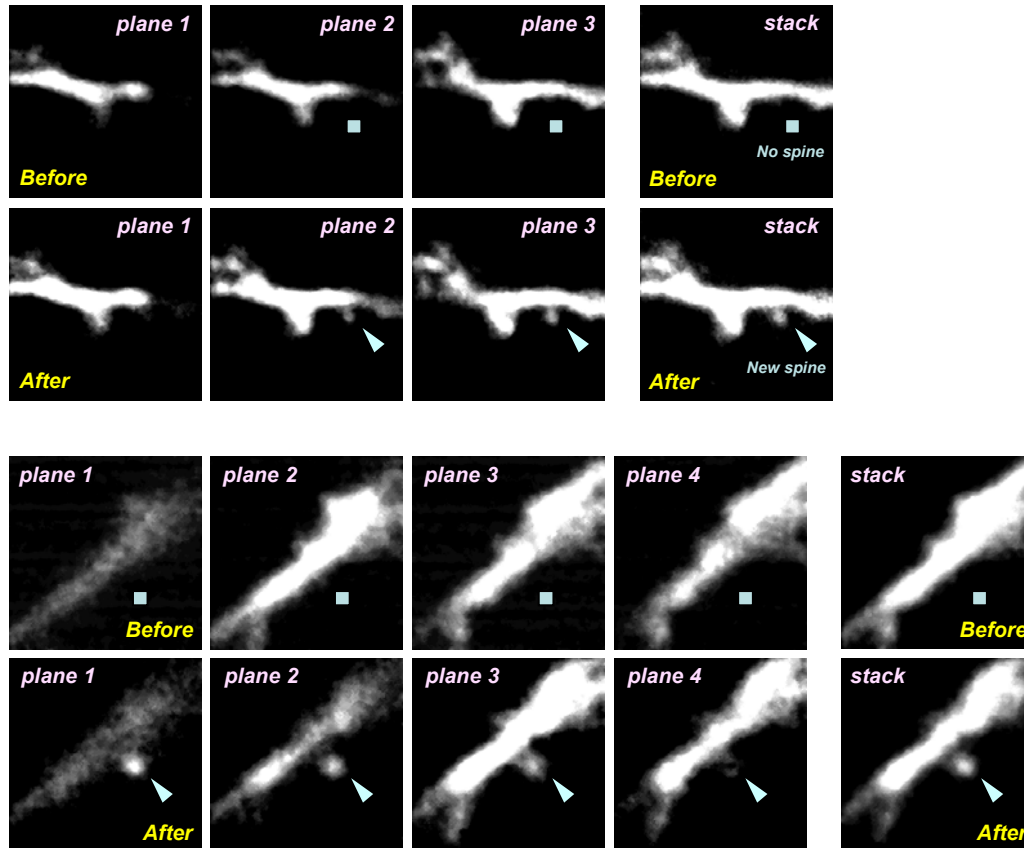
**Supplementary Figure 1 Slice-by-slice analysis of image stacks.**

Image series taken from the same starting and end points at 1 μm spacing (i.e. z-stacks) before and after induction of spine growth are shown slice-by-slice to demonstrate that there were no hidden spines at the site of induced spinogenesis. The corresponding maximal intensity z-projections are shown on the right. Squares indicate the absence of spines in multiple planes at the site at which a spine is induced to grow (arrowheads).
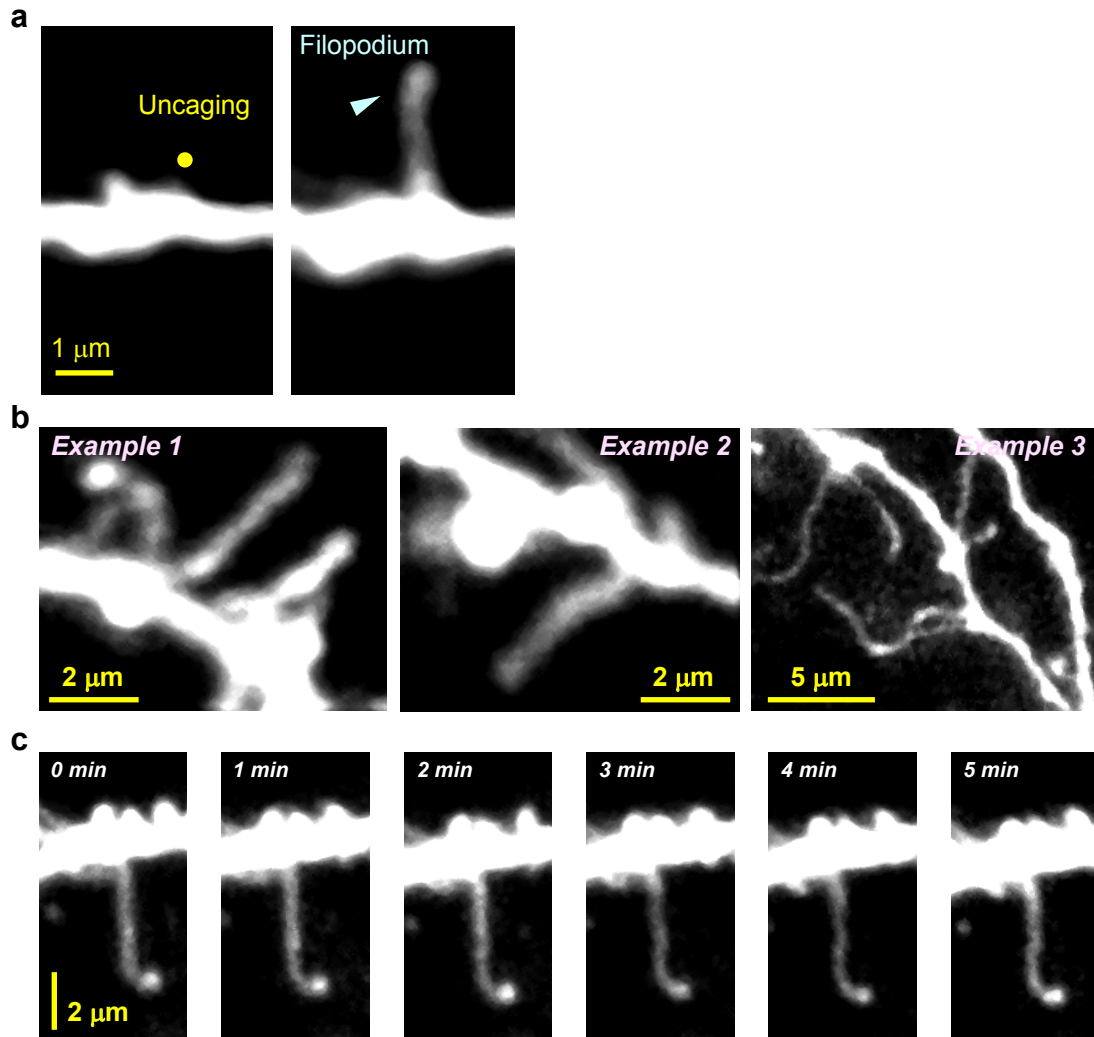
**Supplementary Figure 2 Time-lapse imaging of filopodia.**

(a) An example of filopodium formation induced by glutamate uncaging. **(b)** Three examples of dendritic filopodial protrusions present in basal conditions, demonstrating our ability to detect such thin and long structures. Clustered filopodia (longer than 2.5 µm) were often observed. **(c)** Representative time-lapse imaging of a long and thin filopodium showing stable shape and the length for at least 5 minutes. In such time lapse imaging studies, we found that more than 95% of filopodia (n=70) have life-times of greater than 5 minutes, making it unlikely that a short-lived filopodium was missed during the spinogenesis induction protocol.
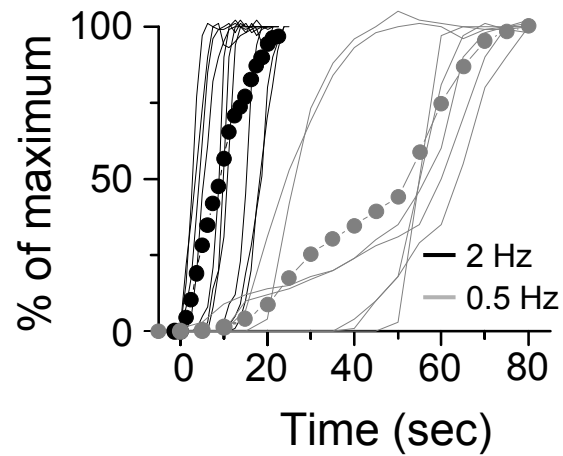
Supplementary Figure 3 Time course of generation of individual spines.
Successful cases of spine formation at 0.5 Hz and 2 Hz were analyzed
separately and are presented by different colors as a function of time during the
induction protocol (Black: 2 Hz, Gray: 0.5 Hz).
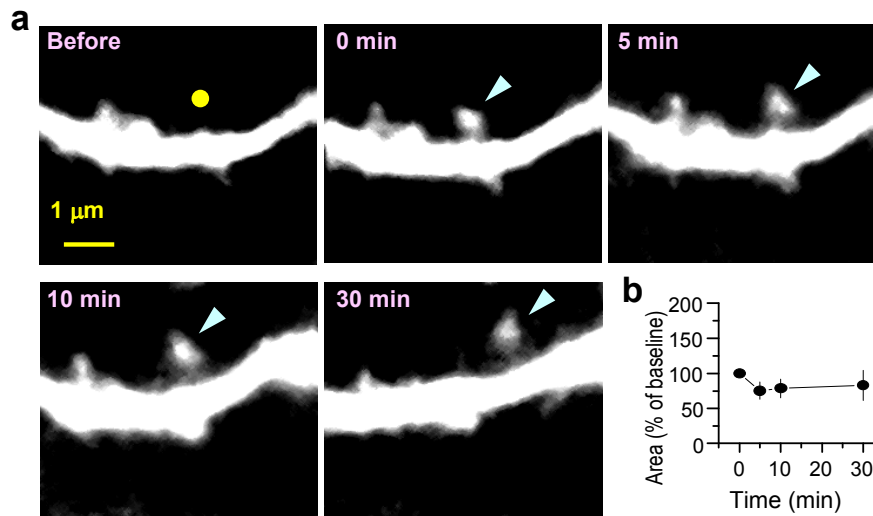
**Supplementary Figure 4 Newly generated spines are long-lasting.**

(a) A representative example showing that a spine induced by glutamate uncaging lasts for at least 30 minutes. Spine images were taken right after spine induction (0 min) and 5, 10, and 30 minutes later. The yellow circle marks the uncaging position and blue arrowheads indicate the new spine. **(b)** Time course of changes in spine head area relative to the first post-induction time point (30 minutes: 83 ± 22 %, n=6). Error bars represent SEM.
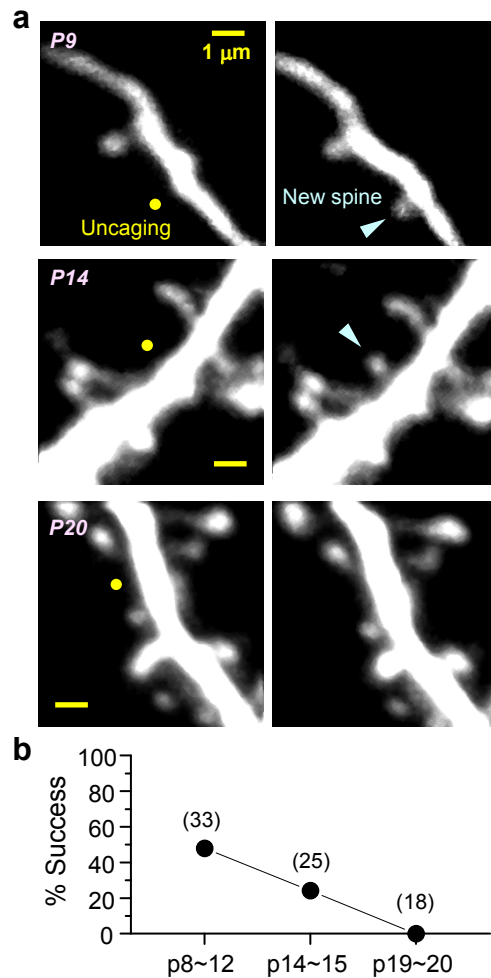
Supplementary Figure 5 Age-dependent modulation of glutamate-induced spine formation.

(a) Sample representative images of glutamate uncaging-induced spinogenesis at different postnatal ages. The same glutamate uncaging protocols (40 pulses at 2 Hz) was tested in acute slices prepared from animals of different ages. Animals of all three age groups were testing using the same experimental setup in a single day. **(b)** Percentage of successful spine generation for tissue isolated from mice of the indicated age ranges. At P14~15, glutamate-uncaging still generated new spines, despite the higher density of existing spines. Induction of new spines failed at P19~20.
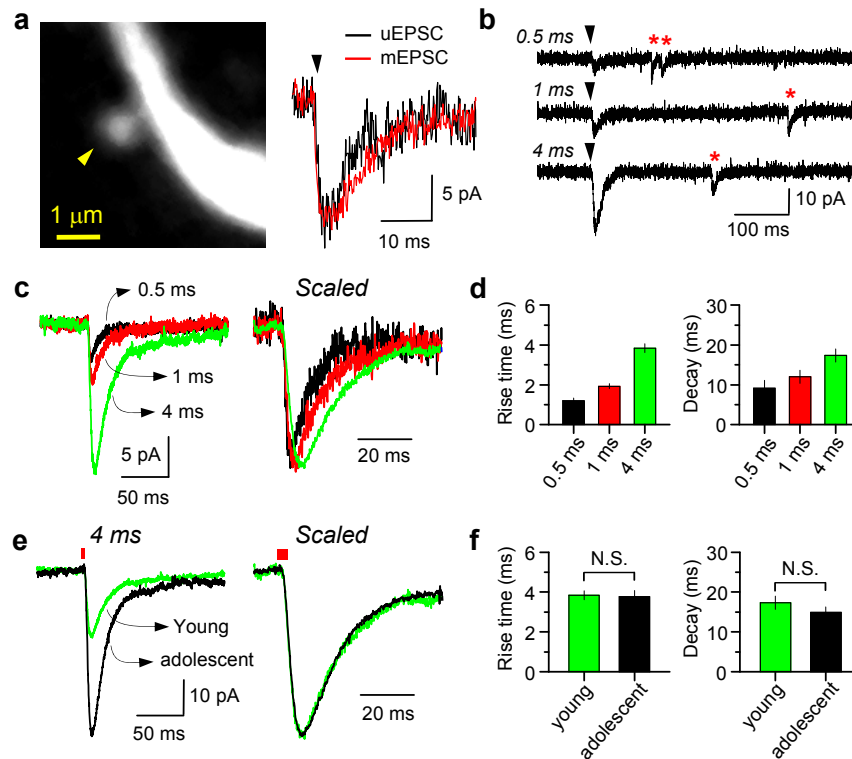
Supplementary Figure 6 Assessing the strength of stimulation delivered by the uncaging pulses.

(a) Glutamate was photoreleased onto a well-isolated spine in acute slices from young animals in the presence of 1 μM TTX. Average uEPSCs evoked by 0.5 ms duration uncaging pulses were normalized and superimposed on the average miniature spontaneous EPSC (mEPSC) recorded in the same cell. Note that the rise and decay kinetics of the uEPSC are similar to those of the mEPSC. **(b)** Example uEPSCs triggered from the same spine head using three different uncaging pulse durations. Black arrowhead and red asterisks indicate uEPSCs and mEPSCs, respectively. **(c)** The average amplitude and kinetics of uEPSCs from many neurons activated by different duration (0.5, 1, and 4 ms) uncaging pulses are compared. **(d)** Summary graphs of rise and decay kinetics for each uncaging pulse duration. The 10~90% rise time was calculated and the decay kinetics were determined from the time constant of a single exponential fit to the decay of the uEPSCs (Rise time: 0.5 ms, 1 ms, and 4 ms: 1.19 ± 0.14 ms, n = 8, 1.93 ± 0.12 ms, n = 10, 3.84 ± 0.22 ms, n=13; Decay: 0.5 ms, 1 ms, and 4 ms: 9.1 ± 1.9 ms, n = 8, 12 ± 1.6 ms, n = 10, 17.3 ± 1.6 ms, n=13). **(e)** Superimposed traces of uEPSCs evoked by 4 ms uncaging from young (P10~12) and adolescent mice (P19~20). **(f)** Summary plots of the rise time and decay kinetics

of uEPSCs from the young and adolescent age groups of mice (Rise time: young and alolescent: 3.84 ± 0.22 ms, n=13, 3.76 ± 0.34 ms, n=9, p>0.5; Decay: young and adolescent: 17.3 ± 1.6 ms, n=13, 14.9 ± 1.3 ms, n = 9, p>0.1). Had the diffusion of glutamate in the extracellular space been substantially different across ages, it would likely have been revealed by changes in the kinetics of the currents produced by this large uncaging stimulus. The lack of kinetic changes suggests similar profiles of glutamate receptor activation.
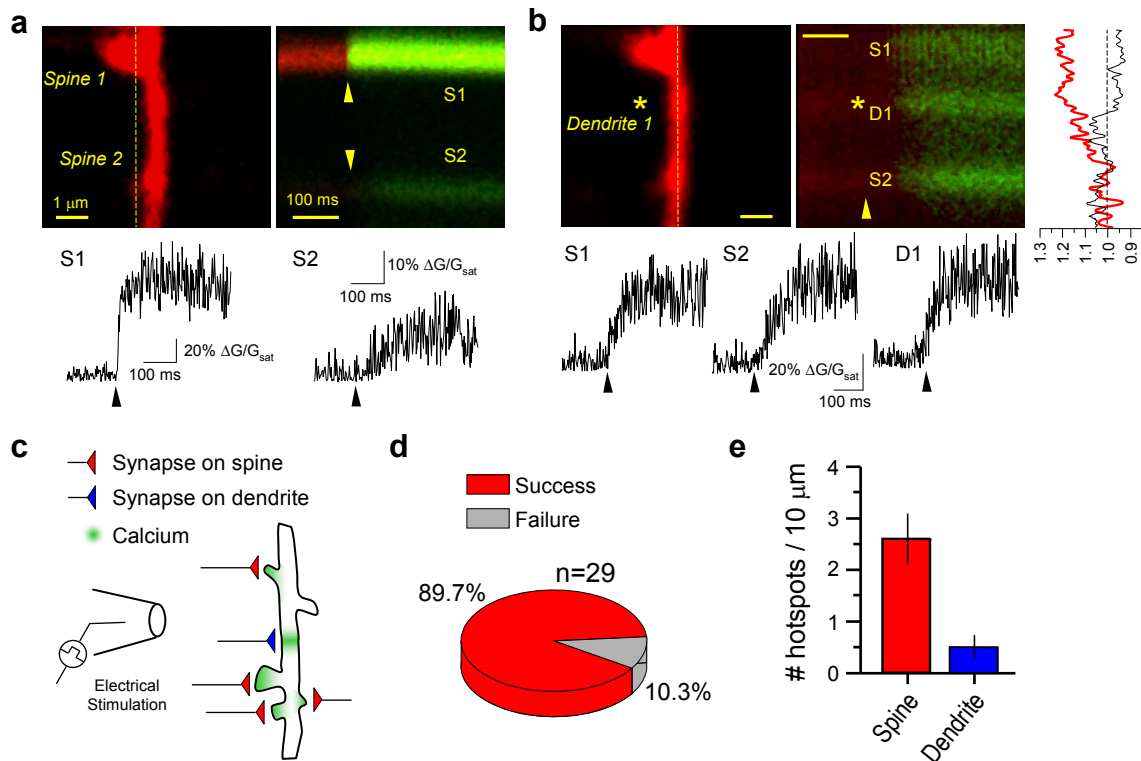
Supplementary Figure 7 Estimating the density of synapses made onto the dendritic shaft.

(a) Dendritic regions containing 2~3 spines were examined from P10~11 day old mice. In the representative example, two spines were observed in a 10 μm-long dendritic segment. Ca^{2+} influx was measured along the dashed line over time. When electrical stimulation was delivered near the dendrite, Ca^{2+} transients (green) were detected in both spines following stimulation (arrowheads). Time course of the Ca^{2+} rise in each spine is plotted below the images. **(b)** When Ca^{2+} was measured along the dendrite in the same experimental conditions, an additional Ca^{2+} hotspot was detected between two spines where no spine could be seen. On the far right is shown the normalized G/R fluorescence ratio along

the line scan for a "success" (red) and "failure" (black) trial. The G/R ratio was normalized to 1 to demonstrate that the fluorescence increase in the upper portion of the dendrite is ~30% greater than in the lower portion, indicating a spatially non-uniform and stochastic Ca^{2+} rise. **(c)** Illustration of how Ca^{2+} hotspots were detected from spines and dendrites. An electrical stimulation electrode was placed approximately 30 μm away from the target dendrite and line scans were performed both across spine heads and along dendrites. **(d)** Pie chart graph showing that about 90 % of spines displayed synaptically-evoked Ca^{2+} signals (n=29 spines, 7 cells). **(e)** Summary graph of the density of Ca^{2+} hotspots observed in spines or on the dendrite shaft. Ca^{2+} hotspots on dendrites were rarely found. A caveat of these experiments is Ca^{2+} transients in the dendritic shaft may be harder to detect than those in spines, resulting in an underestimate of the density of dendritic shaft synapses. However, glutamate uncaging onto randomly chosen sites on the dendritic shaft triggered easily-detected Ca^{2+} transients in the dendrite (Supplementary Fig. 8). On the other hand, the primary difficulty may be in selecting spots on the dendrite for analysis. For example, a thick portion of the dendrite will appear to have a hot spot of influx in the green channel when Ca^{2+} is elevated uniformly in the dendrite – this bias leads to an overestimate of hot spot density. For this reason, it is necessary to identify failures of Ca^{2+} influx based on volume-insensitive measurements such as G/R ratios. However the signal-to-noise of this measure in the dendrite shaft is significantly less than in the spine head, making this analysis difficult. Thus, there are multiple factors that cause the influence the estimate of dendritic shaft synapses. However, ultrastructural analysis of asymmetric synapse distribution in P12 hippocampus found a ratio of dendritic shaft to spine synapses of ~1:1 which is also significantly too low to postulate that nascent spines arise exclusively from dendritic shaft synapses[12].
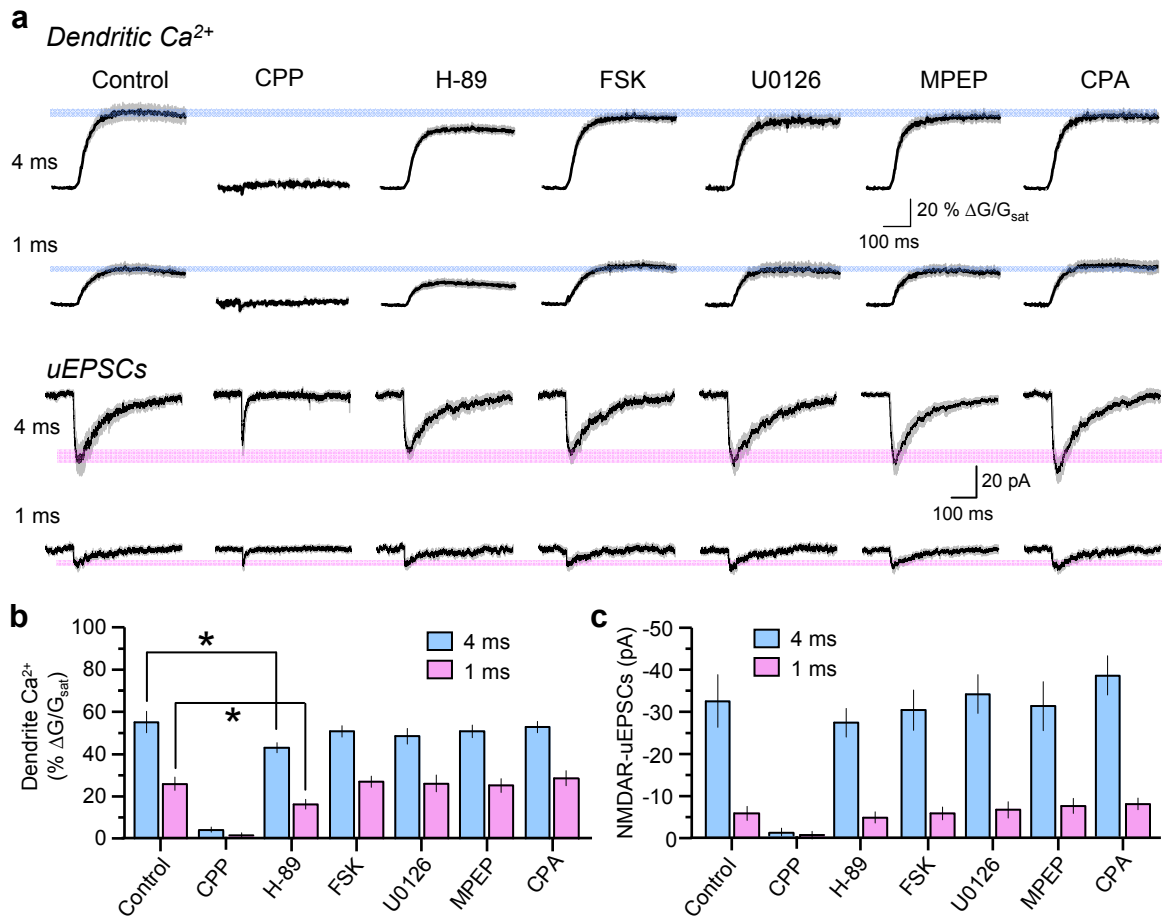
Supplementary Figure 8 Modulation of dendritic Ca^{2+} transients and uEPSCs.

(a) Layer 2/3 pyramidal cells were filled with Alexa 594 (20 µM) and Fluo-5F (300 µM) and voltage-clamped at -60 mV in the absence of Mg^{2+}. MNI-glutamate was uncaged with interleaved 4 ms or 1 ms pulses at a spot ~0.5 µm away from the dendrite as in **Fig. 1**. Fluorescence transients were measure in the dendrite at the location nearest to the uncaging site. uEPSCs were simultaneously measured from the cell soma. The amplitude of NMDAR-uEPSCs was calculated by averaging values the current amplitude 40-60 ms after uncaging. Slices were incubated with individual pharmacological drugs more than 30 min before the recording and the same concentration of drugs was continuously present in the ACSF during experiments. The concentration of each drug was the same as that used in **Fig. 3a**. Blue and red stripes represent the range of values (average ± SEM) of dendritic Ca^{2+} and uEPSCs, respectively, measured in control conditions.
(b-c) Summary histogram of the amplitudes of dendritic Ca^{2+} transients and

NMDAR-uEPSCs triggered by 1 or 4 ms glutamate uncaging pulses. Average response of 3-5 trials (15 sec interval) were used for the analysis from each uncaging spot. The averages and SEM are summarized in Supplementary Table 1.
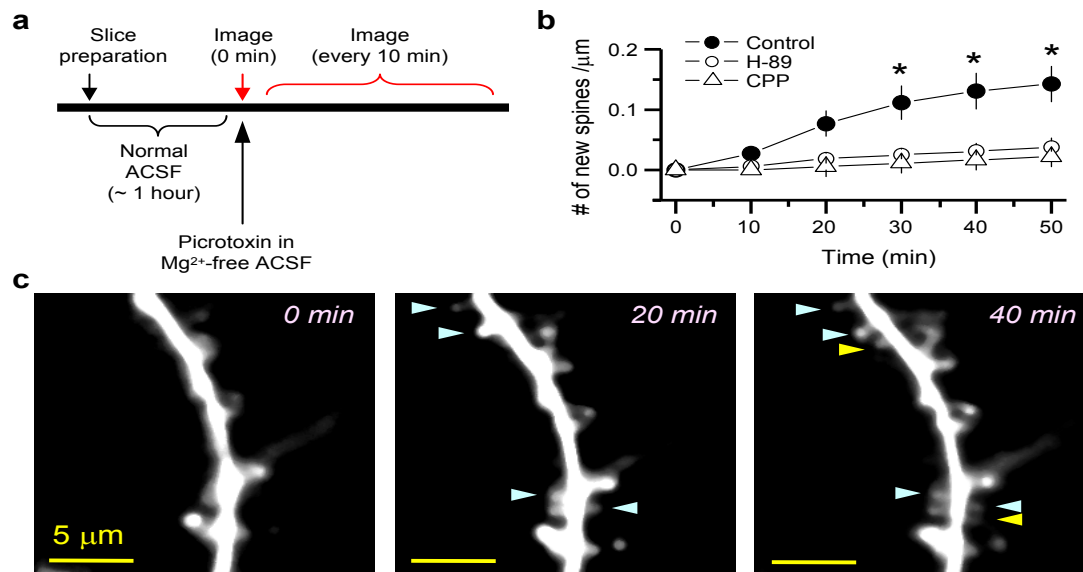
Supplementary Figure 9 Spontaneous spinogenesis triggered by increased NMDA receptor activation requires PKA activation.

(a) Schematic of the experimental timeline. Acutely prepared slices from young mice (P10~12) were kept in normal ACSF for an hour and subsequently transferred to an imaging chamber perfused with Mg^{2+}-free ACSF containing 50 μM picrotoxin. Images were acquired immediately after slices were transferred (0 min time point) and every subsequent 10 min for 50 min. **(b)** New spines were observed to grow when inhibition is blocked and Mg^{2+} block of NMDARs is relieved (50 minutes: 0.14 ± 0.03 new spines/μm, n=13, p<0.005). Application of CPP or H-89 prevented new spine formation in these conditions (H-89: 0.04 ± 0.02, n=8, p<0.05; CPP: 0.02 ± 0.01, n=9, p<0.05). **(c)** Representative images of spontaneously formed new spines. Arrowheads indicate new spines.
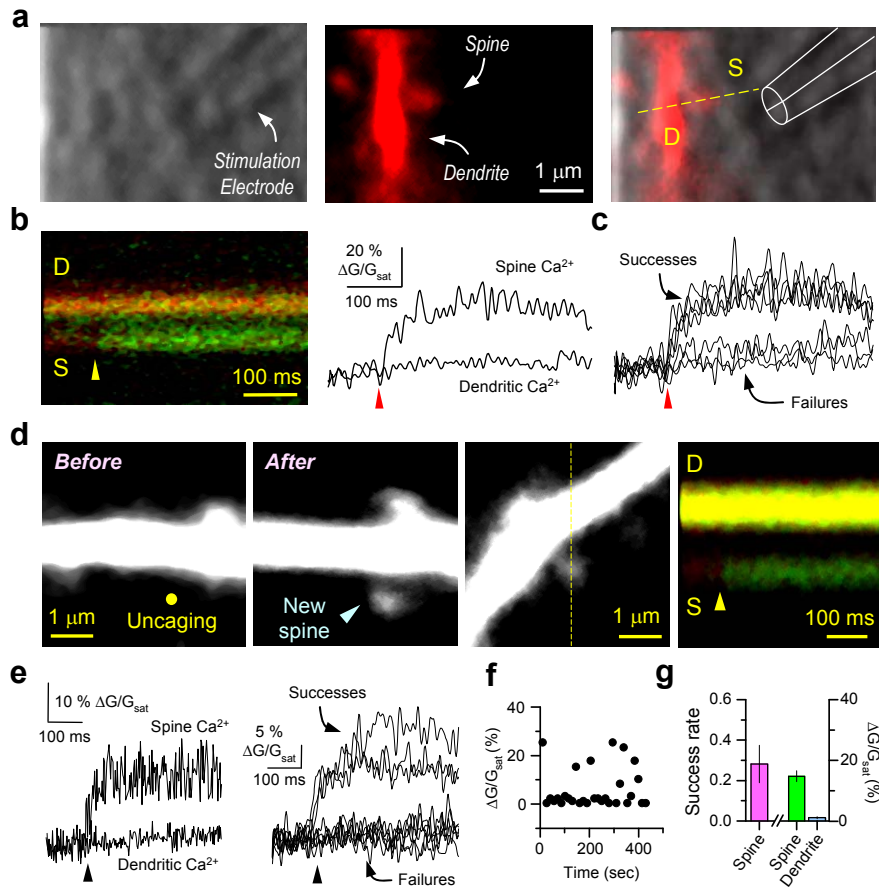
Supplementary Figure 10 Evidence that *de novo* spines induced by glutamate uncaging are associated with functional synapses.

(a) Thin theta glass stimulation pipette (~1 μm diameter of the tip) was localized close to the target spine in order to increase the probability of activating synaptically connected presynaptic axons. The shadow of glass pipette is visible in laser scanning DIC image (*left*). Fluorescence image of dendrite and spine (*middle*) and overlay with the DIC image (*right*) illustrating that the stimulation pipette is placed near the targeted spine. **(b)** Local stimulation triggered Ca^{2+} transients in the spine head (*left*). Fluorescence changes were quantified from the line scan intersecting the spine (S) and dendrite (D) (*right*). The arrowhead indicates the time of stimulation. **(c)** Successive trials showing clear distinction of successful and failures of evoking a Ca^{2+} transient. Figures in **a-c** show the

analysis of a preexisting spine. **(d)** Images of *de novo* spine grow triggered by focal glutamate uncaging as in Fig. 1 (*left* two images). A Ca^{2+} transient was evoked in the newly formed spine by local electrical stimulation (*right* two images). **(e)** Representative traces of fluorescence changes from a new spine head and dendrite (*left*). Superimposed successes and failures of Ca^{2+} signals from the spine head during consecutive stimuli (*right*). **(f)** Time course of successes and failures. **(g)** Average success rate and Ca^{2+} transient amplitude from spines induced to grow by glutamate uncaging (Success rate: 0.28 ± 0.09, n = 5; $\Delta G/G_{sat}$ (%): spine and dendrite: 14.8 ± 1.8 %, 1.0 ± 0.3 %, n = 5). These data were collected approximately 40-60 minutes after initial spine growth. Synaptic Ca^{2+} transients were successfully evoked in 5 out of 12 attempts.

Dendrite Ca^{2+} (% $\Delta G/G_{sat}$)

	1 ms	4 ms
Control	25.9 ± 3.1, n=15	55.1 ± 5.1, n=15
CPP	0.3 ± 1.1, n=7	3.3 ± 1.2, n=7
H-89	16.2 ± 2.3, n=22	43.1 ± 2.4, n=22
FSK	26.9 ± 2.6, n=17	50.9 ± 2.7, n=17
U0126	26.1 ± 3.9, n=11	48.5 ± 3.7, n=13
MPEP	25.1 ± 3.2, n=14	50.8 ± 2.9, n=14
CPA	28.5 ± 3.5, n=16	52.8 ± 2.6, n=16

NMDAR-uEPSCs (pA)

	1 ms	4 ms
Control	-5.6 ± 1.7, n=14	-32.2 ± 6.3, n=12
CPP	-0.3 ± 0.9, n=7	-2.0 ± 0.9, n=7
H-89	-4.5 ± 1.4, n=17	-26.0 ± 3.4, n=18
FSK	-5.5 ± 1.5, n=13	-30.3 ± 4.8, n=14
U0126	-6.4 ± 1.9, n=12	-33.8 ± 4.6, n=12
MPEP	-7.2 ± 1.8, n=11	-30.9 ± 5.8, n=12
CPA	-7.7 ± 1.4, n=14	-38.1 ± 4.7, n=15

AMPAR-uEPSCs (pA)

	1 ms	4 ms
Control	-7.2 ± 1.7, n=14	-42.1 ± 8.4, n=12
CPP	-8.7 ± 2.4, n=7	-31.3 ± 13.8, n=7
H-89	-7.6 ± 1.6, n=17	-35.4 ± 4.2, n=18
FSK	-8.3 ± 2.0, n=13	-37.2 ± 5.4, n=14
U0126	-11.4 ± 1.7, n=12	-44.8 ± 5.4, n=12
MPEP	-9.5 ± 1.9, n=11	-43.8 ± 6.2, n=12
CPA	-11.7 ± 1.9, n=14	-49.4 ± 5.9, n=15

Supplementary table 1

Frequency and duration of uncaging

	4 ms
0.1 Hz	1 out of 11
0.5 Hz	7 out of 29
2 Hz	16 out of 33
5 Hz	7 out of 14

	0.5 ms
0.5 Hz	2 out of 14

Pharmacological drugs

	# of successes
CPP	1 out of 18
Mg2+	3 out of 18
NBQX	6 out of 12
TTX	7 out of 12
CPCCOEt	4 out of 8
MPEP	9 out of 27
AIDA	6 out of 17
CPA	2 out of 16
TG	4 out of 20
KN-62	7 out of 16
KN-93	7 out of 18
K252a	7 out of 16
Forskolin	20 out of 25
H-89	1 out of 19
U0126	3 out of 16
PD98059	3 out of 18

Age of animals

	# of successes
p8~12	16 out of 33
p14~15	6 out of 25
p19~20	0 out of 18

Supplementary table 2